Analysis of the residual stress and bonding mechanism in the cold spray technique using experimental and numerical methods

Michael Saleh [a,*], Vladimir Luzin [b], Kevin Spencer [c]

[a] *Institute of Materials Engineering, Australian Nuclear Science and Technology Organisation, Locked Bag 2001, Kirrawee DC, NSW 2232, Australia*
[b] *The Bragg Institute, Australian Nuclear Science and Technology Organisation, Locked Bag 2001, Kirrawee DC, NSW 2232, Australia*
[c] *BHP Billiton, BMA Coal, 71 Eagle St, Brisbane, QLD 4000, Australia*

A B S T R A C T

In the current study, numerical solutions were used to simulate multi-particle deposition in the cold spray (CS) process, and to investigate some of the physical attributes of the deposition process of AA-6061-T6 particles deposited on an AA-6061-T6 substrate. Earlier experimental results are presented, with varying substrate and cladding combination; a subset of these results is analysed using single particle impact simulation, a more traditional approach in simulations of cold spray, and the smooth particle hydrodynamic (SPH) formulation to simulate multi-particle deposition. In a single particle impact simulation, a strong correlation between temperature and plastic deformation of the CS particles during the deposition process was found. The authors were able to correlate the onset of adiabatic shear instability with pronounced reduction in the flow stress with an inversely proportional relation exhibited for both temperature rise and plastic deformation. In the simulation of multiple particle impact, 400 particles, several bulk characteristics were extracted as through-thickness functions: density, equivalent plastic strain and stress profile. Stress profile from the simulation was contrasted against neutron diffraction measurements of residual stress, along with the analytical model of Tsui and Clyne, and is shown to achieve good correlation and providing validation of the results of simulations. Furthermore it was found that these stresses originate from a delicate balance between (a) the strain rate hardening and thermal softening and (b) the shot peening effects induced by the impact of CS particles. Analysis of particle morphologies in the simulation suggests a strong influence of temperature rise at the periphery of CS particles during deposition and dynamic recrystallization with the strong jetting of molten metal allowing for inter particle mixing and substrate adhesion.

© 2014 Elsevier B.V. All rights reserved.

1. Introduction: cold spray

Cold spray is a material deposition technique in which particles of metal powder are accelerated up to speeds of 500–1000 m/s by injecting them into a carrier gas stream which impacts a metallic substrate and is bonded to the surface. In this process metallurgical bonding can occur only when the particle velocities reach a critical limit that is defined by the material properties and process conditions. The impact of particles onto a substrate and cohesion of the particle on a substrate, or, in other words, formation of metallurgical bonding, is a key part and a basis of the CS or the kinetic spraying technique.

There are a number of major ideas [1–6] as to the deformation sequences and the bonding mechanism associated with the CS technique. The major theories look at the interface temperature and the large adiabatic instabilities developed during the plastic deformation of both the particles and the substrate [2,3]. Other theories [2,7] have concluded that successful bonding can only occur if a critical velocity is reached which governs both the contact area and the contact time.

A factor and a distinctive feature of the CS process, which is closely related to the coating integrity and linked to the boding mechanism, is the residual stress that builds up in the material

* Corresponding author. Tel.: +61 297179883; fax: +61 297179225.
E-mail address: michael.saleh@ansto.gov.au (M. Saleh).

during spraying. It was shown in several studies [8–11] that CS produces compressive residual stress, which can be beneficial when it is of moderate magnitude. However, large compressive stresses can also lead to the coating failures (e.g. through delamination) and the question of effective stress control through tuning the spray process parameters and material properties is important, provided that bonding is not compromised. Thus, understanding of the bonding mechanism together with the stress formation might be decisive for improving the overall integrity or performance of the coating

In earlier works [6,12,45,46] the authors attempted to interpret the measured values based on the kinetics of the spray process and material properties without finite element calculations, but the focus of the current study is the single- and multi-particle impact using finite element (FE) simulation. These can demonstrate some microscopic features of the particle bonding mechanism and the local stress distribution on a 60 μm thick substrate. In this study we also present measurements of residual stress in macroscopically thick AA-6061-T6 CS coatings, 3–4 mm thickness, produced using two slightly different spraying techniques. The experimentally determined through thickness stress profiles by neutron diffraction on macroscopically thick coatings were used to validate FE calculations made for 100 μm thick coatings. This was done by using the progressive deposition model of Tsui and Clyne [7] to correlate the experiments and simulations. Combining complementary approaches, experimental and modelling, some new insight into CS deformation was achieved.

2. Sample production and characterization

Two samples were of interest and these were characterized by a similar particle speed of ~600 m/s, although they were sprayed by two different CS techniques. The first sample was produced by a kinetic metallization (KM), a commercially available low-pressure CS system that uses a convergent barrel nozzle and operated under choked flow conditions with the gas speed through the nozzle barrel ~Mach 1. The AA-6061-T6 powder, with 15 μm diameter spherical particles produced by atomisation, was used to feed the spray system and deposited the particles onto an AA-6061-T6 substrate as shown in Table 1.

For the KM samples, the speed was estimated using Dykhuizen and Smith formalism [37] through velocity integration along the nozzle barrel. The particle drag coefficient was calculated according to the local Reynolds number and Henderson's correlation by evaluating the particle nozzle exit velocity based on the gas stagnation temperature, pressure, and the He gas thermodynamic properties using a 1-dimensional isentropic model. In the case of the samples sprayed using the supersonic CGT system, the particle exit velocities were calculated using the commercially-available computational fluid dynamic code FLUENT 3D.

The coatings were characterized by optical metallography in order to measure the amount of plastic deformation in the cold sprayed material. It was found, by assuming initial spherical shape of the particle and fitting deformed shape with an ellipsoid, that for both samples the
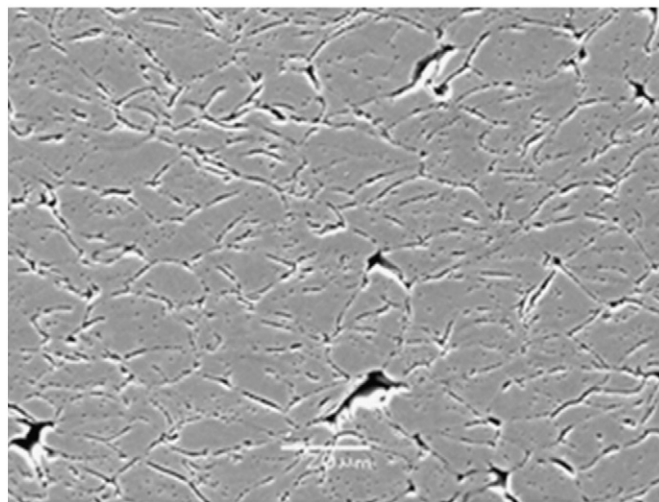
Fig. 1. Microstructure of the KM AA-6061-T6 on AA-6061-T6 system with the coating material showing the elongated grains (grey areas are single phase Al with limited porosity appearing as black areas). The image is taken 0.1 mm above the substrate/coating interface.

plastic deformation was about the same, 50%, as demonstrated in Fig. 1. The analysis of aspect ratios $l_{\parallel}/l_{\perp}$ of multiple particles (~50 measurements for each sample) allowed the authors to evaluate the average equivalent plastic strain, $\bar{\varepsilon} = \frac{2}{3} \ln \left(\frac{l_{\parallel}}{l_{\perp}} \right)$. Exact values are reported in Table 2 together with measured densities, measured using Archimedes' method, and the Young's modulus, measured using the impulse excitation technique [44] according to ASTM standard E1876, these methods were utilised in earlier studies of the cold spray technique by the current authors [45,46]. The values are shown as percentages of bulk values.

3. Neutron stress measurements

The neutron diffraction residual stress measurements were carried out at the OPAL research reactor, Australian Nuclear Science and Technology Organisation, using the KOWARI strain scanner. A gauge volume of $0.5 \times 0.5 \times 18$ mm was used in allowing to measure the stress profile with fine enough through-thickness resolution. At the same time it was sufficient to measure strains with statistical uncertainty $\sim 5 \times 10^{-5}$, within reasonable experimental time.

A 90° geometry ($2\theta_B \sim 90°$) was chosen to rectify localisation of the gauge volume. To maintain this, the take-off angle $2\theta_M$ of the Si (400) monochromator (or the neutron wavelength) was varied according to the material (see Table 3). The measurements were done in several different through-thickness locations to cover the entire sample thickness, forming a line profile with 0.3 mm spacing between points. For each measurement point, d-spacings (diffraction peak positions) were measured in the two principle directions, normal to the surface and in-plane. From the measured d-spacings, in-plane stresses were calculated using the assumption of a balanced biaxial plane stress state, following the procedure described in [48]. The diffraction elastic constants used for stress calculation were computed using the self-consistent method of Kröner [47], and are reported in Table 3.

Table 1
Materials and process parameters used for cold spray.

Powder material/ substrate	Cold spray process	Average particle size (μm)	Driving gas	Driving pressure (kPa)	Nozzle temp. (°C)	Nozzle gas speed (m/s)	Calc. impact speed [m/s]
AA6061-T6/AA-6061	KM	15	He	620	~140	1025	585
Pure Al/Mg	KM	15	He	620	132	1025	585

Table 2
Coating density and Young's modulus as a percentage of their equivalent bulk values.

Powder material/substrate	Impact strain	% bulkdensity	% bulk Young's modulus
KM AA-6061/AA-6061	0.6 ± 0.2	93.6 ± 0.6	69.6 ± 0.7
KM Pure Al/Mg	0.47 ± 0.16	94.6 ± 0.4	80.9 ± 0.7

To separate stresses originating from the cold spray process from pre-existing stresses (*e.g.* residual stress from cold rolling of the substrate), neutron stress measurements were done on the uncoated substrate, as shown in Fig. 2. They were treated as separate samples and measured using the same procedure. In subsequent data analysis, the stress profiles measured in uncoated substrates were subtracted from the stress profiles of the coated samples.

4. Analysis of experimental stress profiles

The obtained through-thickness stress profiles were fit to the progressive deposition model of Tsui and Clyne [7]. This powerful analysis served several functions as described below.

4.1. Data quality evaluation

Experimentally determined residual stress distribution, as a solution of an elasticity theory problem considered in plane-stress formulation, should fulfil stress and momentum balance conditions and boundary condition. Fitting experimental distribution to a model function that comply with all of the above by default is a powerful tool to check quality of data, for example, to determine possible outliers.

4.2. Separation of thermal vs. kinetic effects

This separation is possible through analysis of the residual stress data due to their different functional dependencies and thus their contributions to the resultant stress profile. Essentially, the model involves two components that describe the stress state in the CS process and two fitting parameters that prescribe their contributions.

The first fitting parameter characterizes the coating deposition process and quantifies the amount of stress due to formation of every new layer on the top of the system of the previously sprayed layers, plus the substrate. It is called deposition stress σ_d and for CS this stress is compressive due to dominance of a peening process. The second fitting parameter describes post-spray cooling to room temperature and is characterized by a thermal misfit term $\Delta\varepsilon_{th} = \Delta\alpha\Delta T$. This term is significant for coating/substrate combinations in which thermal expansion coefficient mismatch $\Delta\alpha$ or/and the temperature drop ΔT are large. Analysis of the experimental stress profiles in terms of the model allows separation of σ_d and $\Delta\varepsilon_{th}$, and extremely helpful to clarify a physical path to stress formation and a quantitative evaluation of different processes. In earlier studies [6] it was used to demonstrate the peening nature of stress in CS coatings, quenching origin of stress in plasma spray coatings and their combined effect in HVOF (high-velocity oxi-fuel) coatings
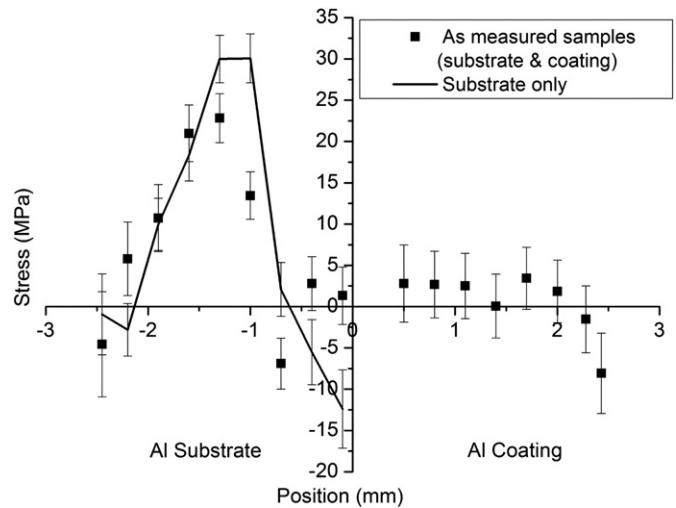
4.3. Elimination of the geometrical factors

When fitted to the model, experimental results can be compressed into two fitting parameters and these can be used for stress predictions

Table 3
Instrument settings and material constants for the measured reflections.

Reflection	d, Å	$2\theta_M$	λ, Å	$2\theta_B$	S_1, TPa^{-1}	$\frac{1}{2}S_2$, TPa^{-1}
Mg (211)	1.03	65.0°	1.36	90.1°	−6.55	28.94
Al (311)	1.22	79.8°	1.72	89.5°	−5.16	19.57

Fig. 2. Through-thickness stress profile as measured and substrate only stresses. The latter were subtracted from the former in Fig. 3.

using any chosen combination of coating and substrate thicknesses. This predictive recalculation approach was used to relate results obtained experimentally in thick (~1 mm) and results of simulations in thin (~30 μm) coatings.

4.4. Elimination of dependence on material of substrate

In a similar way the use of fitted parameters allows the authors to reconstruct the stresses for any combination of substrate material. However, care should be taken to make sure that substrate material is not modified by spraying process. For example, the very top layer (~0.2 mm) of substrate can also be peened in the process of deposition but when this layer is small in comparison with the total thickness (~2 mm) then this effect can be considered negligible, but not otherwise.

5. Numerical simulation: smooth particle hydrodynamics (SPH)

Although the SPH method was originally developed by the astrophysical community, Gingold and Monaghan [17] and Lucy [18] in order to solve large gas-dynamics problems, there has been a drive to apply the SPH method to other areas such as fluid-dynamics [14], high velocity impact [15] and metal cutting [16]. The SPH method is based on a collective movement of material particles in a similar fashion to fluids and it can be thought of as a Newtonian fluid with the associated conservation equations. . There are a number of advantages of the SPH method that qualify it for application to the CS technique, namely:

(i) Advection of the material is handled well as there is no material movement across any element as in the case of Euler or Arbitrary Lagrangian Eulerian (ALE) formulation.

(ii) There is no need to explicitly track the contact interfaces as in the case of the Lagrangian formulations, hence issues of choice of contact algorithms are avoided.

(iii) The discretised particle domain allows for the computational solution of largely deformed structures without the associated problems of severely deformed elements, reduced time steps in the explicit codes and the need to rezone and remesh the Lagrangian formulation.

(iv) SPH can also handle complex geometries with reduced requirements for partitioning

(v) The mass conservation properties of the SPH method also ensure that both the energy and the momentum of the simulation are conserved, unlike ALE or Eulerian methods where the advection of the material may cause a loss of energy.

(vi) The discrete nature of the SPH formulation lends itself to rapid scaling which is an advantage when modelling the μm sized CS particles.

In the current study, the SPH formulation model was used to simulate particle impact and adhesion onto a substrate surface and the accompanying deformation. The SPH was used to negate two significant problems with the Lagrangian method: the severe element distortion associated with the high strain rate deformation of the particles and the element/mesh sensitivity of the adiabatic instability as reported by Bae et al. [3]. The SPH method is an element free Lagrangian formulation whereby the structure is represented by a series of material points with a smoothing kernel used to interpolate between each material point. This influence function effectively relates neighbouring particles in order to compute the stress and strain relations. From the single particle analysis, the SPH method was extended to model a multiple layer system comprised of multiple particles on a larger substrate domain.

5.1. SPH in LS-DYNA: material model

A simulation software package, the hydrocode LS-DYNA [20], was previously used for the analysis of high speed ballistic impacts [21]. Since there are many parallels between the CS and the ballistic impact processes, both being highly transient regimes requiring non-linear explicit analysis, the SPH was recognised as highly suited to the analysis of the CS process. The brief explanation of the mathematical formulations underpinning the SPH technique can be found in Appendices 1 and 2.

Studies that have looked at the numerical simulation of the CS method using the solid Lagrangian element approach [1–4] failed to evaluate the adhesion of the particle to the surface of the substrate within the simulation. In the current study the authors have exploited numerical behaviours of the SPH method to achieve material deposition. The review paper by Liu et al. [22] highlights the issue of inter-particle force (IFF) and considers the attractive forces between different SPH particle pairs and their contribution to the interface tension. For fluids, the van der Waals forces can be transformed to SPH attraction forces between neighbouring particles through the use of a suitable EOS. Analogous to that observation, using a solid EOS, like Mie–Grüneisen, would similarly produce attraction forces that mimic interatomic bonds for the case of Al–Al CS deposition thus allowing the authors to deduce the residual stresses. Fundamental to achieving the adhesion was the realisation that single particles, when tested separately, did not adhere to the substrate, but, when nestled within a collection of particles identified using the same part number in the simulation the resultant internal energy is large enough to ensure adhesion upon impact. Based on the previous experience with ballistic problems [21] and on initial sensitivity studies, the most appropriate SPH options, features and parameters for conducting the successful analysis of the CS problem were identified. Although a number of particle approximations are available within LS-DYNA, the symmetric formulation (IFORM = 2) was found to be the most appropriate as it is mathematically tractable and the model exhibited less tensile instabilities compared to the other formulations.

5.2. High strain rate constitutive model: Johnson–Cook

The three parameter Johnson–Cook (JC) constitutive model [23] was used to compute the flow stress of the materials under high strain:

$$\sigma_{eq} = \left[A + B\varepsilon^n\right]\left[1 + C1n\dot{\varepsilon}_*\right]\left[1 - (T_*)^m\right] \tag{2}$$

where σ_{eq} is the flow stress, ε is the effective plastic strain, $\dot{\varepsilon}_* = \dot{\varepsilon}/\dot{\varepsilon}_0$ is the dimensionless plastic strain rate, $T_* = \frac{T - T_0}{T_{melt} - T_0}$ is the homologous temperature and A, B, n, C and m are material constants.

This phenomenological model accounts for (i) the increase in yield stress due to strain hardening through dislocation pile up (first bracket), (ii) the increase in yield and tensile strength with increased strain rate (second bracket) and (iii) the thermal softening of the material (third bracket) due to thermal-plastic instability. This model was successfully used to model several high rate deformation process like shot peening [24] (strain rate 10^4 s^{-1}) and laser shock peening [25] (strain rate 10^6 s^{-1}).

Owing to the highly transient nature of the high strain rate deformation typical of CS, the temperature increase is assumed adiabatic, and can be calculated according to the following relation:

$$T = \int_0^\varepsilon \chi \frac{\sigma_{eq} d\varepsilon}{\rho C_p} \tag{3}$$

where, C_p is the specific heat of the material and ρ is its density. The Taylor–Quinney coefficient, χ, has been set as 0.9 since high strain rate deformation is generally characterized by the bulk conversion of the plastic work into adiabatic heating of the specimen.

5.3. Equation of state (EOS): Mie–Grüneisen

In many instances (e.g. the class of high rate impact problems) the stresses generated from the particle impact far exceed the dynamic yield strength of the material. Additionally, with increasing pressures the wave velocity through the material will proportionally increase [39]. These two conditions will give rise to the formation of shock waves. As such the material begins to behave more like a fluid; this may be accompanied by a phase transition. In many instances, though, phase transitions are neglected for the purpose of constructing a partial EOS, while also neglecting the effect of thermal conduction for short duration events (microseconds).

The EOS relates the pressure to the density and internal energy, and during the deposition process it is the large internal energy generation that gives rise to the hydrostatic stress within the model.

The Mie–Grüneisen EOS for compressed materials as it appears in LS DYNA, defines pressure in terms of a cubic shock velocity–particle velocity:

$$p = \frac{\rho_0 C_{sp}^2 \mu \left[1 + \left(1 - \frac{\gamma_0}{2}\right)\mu - \frac{a}{2}\mu^2\right]}{\left[1 - (S_1 - 1)\mu - S_2 \frac{\mu^2}{\mu + 1} - S_3 \frac{\mu^3}{(\mu + 1)^2}\right]} \tag{4}$$

Table 4
Material data for the AA-6061-T6 used in the simulation.

Material properties	
Density ρ, (kg/m^3)	2770
Shear modulus G (GPa)	26.4
Young's modulus E (GPa)	68.9
Poisson's ratio ν	0.33
Taylor Quinney coefficient χ	0.9
Specific heat C_p (J/kg K)	896
Johnson–Cook model parameters [26]	
A (MPa)	324
B (MPa)	114
Strain hardening constant, n	0.42
Strain rate hardening constant, C	0.002
Thermal softening constant, m	1.34
Reference temperature T_r, (K)	300
Melting temperature T_m, (K)	925
EOS data [27]	
Bulk sound speed C_{sp} (m/s)	5240
Hugoniot slope coefficient, S_1	1.4
S_2	0.0
S_3	0.0
Initial Gruneisen gamma value, γ_0	1.97

while for expanded materials the relation is as follows:

$$p = \rho_0 C_{sp}^2 \mu + (\gamma_0 + a\mu)e. \tag{5}$$

The parameters S_1, S_2, and S_3 are the coefficients of the slope of the Hugoniot curve, C_{sp} corresponds to the speed of sound through the solid, ρ_0 and γ_0 are initial density and the Gruneisen parameter respectively, a is the correction factor for γ_0, e is the internal energy and $\mu = \frac{\rho}{\rho_0} - 1$.

6. Geometry and parameters of the computational models

The simulation setup is analogous to the experimental procedure outlined in Section 2 as an idealised stacking arrangement is employed to simplify the simulation. The simulations centred on the impact of 15 μm AA-6061-T6 particles onto an AA-6061-T6 substrate with the estimated particle exit velocity of 585 m/s and this is used herein as the initial velocity boundary condition. Material data used for the simulations is shown below in Table 4.

6.1. The Lagrangian solid element approach

The solid Lagrangian element approach was taken initially in an attempt to model the CS using 3D solid elements, in line with other FE studies [1–4]. Constraints in both rotational and translational modes along the bottom surface and the periphery were applied to the substrate. It is useful to model a single particle to validate the material models and to ascertain the particle behaviours. This method is suitable for moderate plastic deformation, but beyond these early stages of the impact simulation severe element distortions lead to unphysical contact, loss of accuracy and severe deterioration in the time steps. Some of these problems were remedied by using 2D re-meshing techniques but these quickly overwhelmed the simulation through the sheer number of elements; additionally only tri elements can be utilised in solid re-meshing and their propensity for shear locking is widely noted, making them unsuitable. Considering these difficulties, it was not favourable to model the impact of multiple particles using this method.

6.2. SPH: single- and multiple-particle simulation

The SPH method was used to go beyond the single particle simulations and to attempt to capture the bulk properties associated with multiple passes of a CS nozzle. Through a number of iterations the final model is comprised of 400 particles with 1,000,000 SPH elements distributed along 4 staggered, horizontally aligned layers. The spatial distribution of the SPH particles is uniform with a cubic lattice (CL) arrangement. Diehl et al [29] investigated variation in the packing methods and highlighted that initial conditions that utilised cubic and hexagonal closed packed are more favourable than the most popular arrangement, CL, due to the preferred geometrical axes exhibited in CL

configurations which may skew results for highly perturbed particles. The authors where unable to investigate the sensitivity of these parameters on the models owing to the limitations of the software but it is prudent to highlight this facet of the SPH technique. Within each layer particles are rendered in square grid and in each row they are staggered by a value equal to 0.7 D where D is the diameter of each particle. Different layers were shifted by the half-period of the grid/mesh/lattice in the particle layer. The final pictorial arrangement with dimensions and staking arrangement of the particles in the multiple-particle CS deposition mode is shown in Fig. 4

The regular arrangement of particles in the model is an idealised approximation of the random staggered formation that occurs in the real process and seen is SEM analysis of cold sprayed materials [6] and in the current study. The choice of the regular arrangement ensured more uniform spatial distribution of the SPH particles during modelling as opposed to a truly random choice of particle position/location with large statistical fluctuations. In our case, with the number of particles being limited by computing capacity, statistical variation would be too great (or number of necessary statistical trials would be too great) to statistically provide meaningful result. The current model allows the authors to capture some physical realities of the process allowing the particles to interact more realistically with both hoop and radial stress being present during the deposition. The contact between the CS particles and the substrate is handled automatically with no requirement for additional contact cards.

The SPH numerical method is only supported for the explicit simulations hence in order to compute a 'springback' type simulation any dynamic effect must subside to ensure convergence to an equilibrium state. The simulation was thus continued for a considerable period beyond the initial deposition of all the CS layers. Intermittently the results were interrogated to look at the elemental stress histories and ensure no or limited stress oscillations upon termination of the simulation.

7. Residual stress by neutron diffraction: experimental results

The through-whole-sample-thickness in-plane residual stress profiles, determined by neutron diffraction, are shown in Fig. 3 for two samples. Al coating is in slight compression that is characteristic for CS coatings unless it is overpowered by residual stress generated by thermal expansion discrepancy between coating material and substrate material, this was also shown in earlier studies [45,46]. The two Al coating stress profiles are similar, regardless of the substrate material, because of similarity in thermal and mechanical properties of Al and Mg. The uncertainties of 5–10 MPa achieved in the stress determination are due to neutron counting statistics and positioning errors. They are typical of this type of experiment, though might be perceived large because of small absolute values of stress (Table 5).

The stress profiles were treated within the analytical framework of the Tsui and Clyne model, described in Section 4, and the two fitting parameters σ_d (deposition stress) and $\Delta\varepsilon_{th}$ (thermal mismatch) were
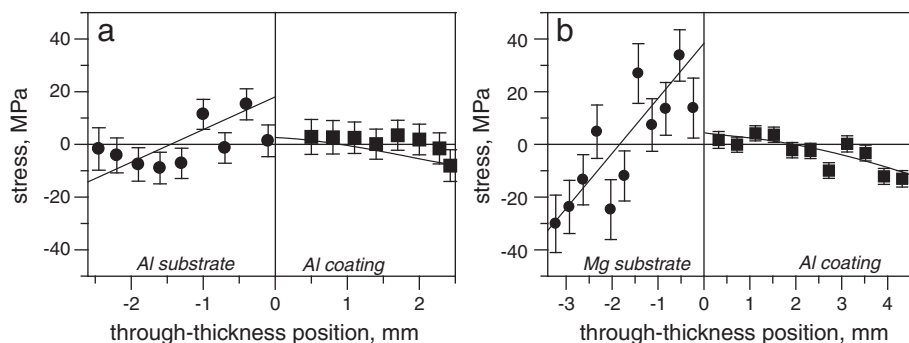

Fig. 3. Stress profiles in AA-6061-T6 cold spray coatings sprayed on (a) Al substrate and (b) Mg substrate. Symbols are the measured values, and solid lines are the progressive deposition model fit [7].
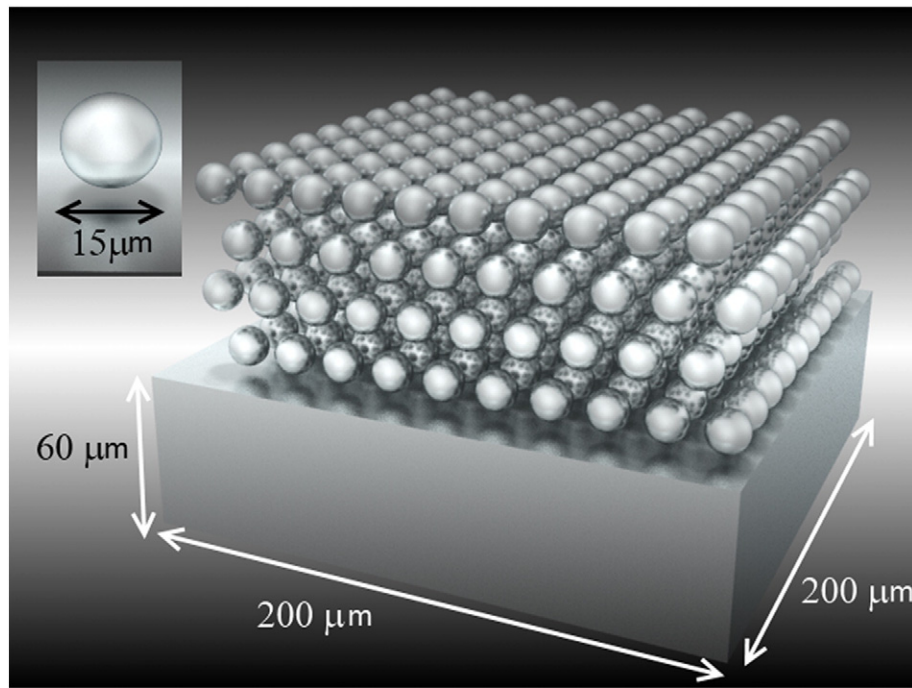
Fig. 4. Dimensions and staking arrangement of the particles in the multiple-particle cold spray deposition model.

determined through curve fitting while parameters such as coating thickness and elastic modulus are taken from experimental measurements. The fitting parameters are given in Table 6 and the corresponding stress profiles are shown in Fig. 10 as solid lines. The experimental data and fits, considered together, demonstrate good quality of experimental data and fit: stress and stress moment balance conditions are fulfilled and χ^2 is around 2.

When deposition stress and thermal mismatch are separated the thermal vs. kinetic effects can be judged easily. Because thermal mismatch between material of substrate and coating is negligible, even for Al/Mg combination, $\Delta\varepsilon_{th}$ is small, gauged by error bar scale. Therefore, the stress profiles are almost entirely determined by σ_d. The two model parameter, when fitted, eliminates coating/substrate thickness, influences the material of the substrate and can be compared naturally as shown in Table 6.

8. Results of simulations

The impact of a single Al particle onto the Al substrate results in similar profiles in both the solid element and the SPH elements, as shown in Fig. 5. The two models show comparable radial jetting of the CS material and moderate cratering of the substrate surface. Results of the multi particle SPH simulation are thus comparable to the Lagrangian simulations and are less sensitive to particle/mesh size as outlined by Li et al. [31]. Complementarity of these methods was used to derive the temperature–time history of a single particle by the Lagrangian solid element simulation rather than the SPH simulation, as temperature data could not be deduced readily from the SPH simulation.

Temperature–time diagrams, shown in Figs. 6 and 7, demonstrate that local temporal temperature can exceed the melting point of aluminium in areas of particle–substrate contact. The increase in temperature is intrinsically linked to the loss of shear strength leading to the

varied morphologies of the particles in the through thickness of the clad layer.

In order to analyse the residual stress within the model and compare the results to those reported in the experimental study, the LS-DYNA data was externally processed in MATLAB [28]. In order to correlate the modelling results to the experimental data the stress profiles were extracted by (a) subdividing the cold sprayed substrate into thin horizontal 'bins' or 'boxes' with the through thickness dimension being smaller than the in-plane dimension, and (b) taking an average stress for the elements falling into each of the aforementioned bins. For this analysis of the CS layers and the through thickness stress profile of the FE model, only a small, centrally spaced specimen is chosen in order to alleviate any boundary edge effects which may skew the stress results. The truncated point cloud and a rendered representation are shown in Fig. 8. A total of 45 through thickness sampling 'bins' or 'boxes' of size $10 \times 10 \times 2\,\mu m$ were analysed with respect to the number of particles in each *box-plane* and the average stress over each box was extracted. In evaluating the stress profile it is pertinent to emphasise the shot peening effect in the substrate material: a thin peened layer that extends to a depth of approximately 5 μm and where large compressive stresses are present is observed next to the interface, while deeper lying aluminium substrate material exhibits no plastic deformation and moderate tensile stresses.

Because the coating materials experience the same peening, some compressive residual stress is expected to be induced in the coating, though somewhat partially modified (alleviated) by stress annealing due to temperature effects. These two contributions to the resultant stress distribution were separated and characterized using the same Tsui and Clyne model. Due to the model's ability to eliminate geometrical factors and substrate material factor as outlined earlier, fit of the stress profile in Fig. 9 can be recalculated to the sample geometry of

Table 5
Estimated impact parameters based on linear momentum transfer.

Powder material/substrate	Calculated impact speed [m/s]	Average impact strain	Impact duration [s]	Average strain rate [s^{-1}]	Average impact pressure [MPa]	Maximum impact pressure [MPa]
KM AA-6061/AA-6061	585	-0.6 ± 0.2	2.3×10^{-8}	2.7×10^{7}	680	4520
KM Pure Al/Mg	585	0.47 ± 0.16	1.9×10^{-8}	2.44×10^{7}	828	4519

Table 6
Fitting parameters of the model [13] and the quality of fit of the experimental data.

Powder material/substrate	Thickness	$\sigma_d \pm$ error, MPa	$\Delta\varepsilon_d \pm$ error, $\times 10^{-6}$	$\Delta\varepsilon_{th} \pm$ error, $\times 10^{-6}$	χ^2
KM, AA-6061/AA-6061	2.5/2.6 mm	-9 ± 2		3 ± 200	2.2
FE simulation, AA-6061/AA-6061	100 μm	-10 ± 7		0	2.0
KM, Al/Mg	4.6/3.4 mm	-17 ± 7	-620 ± 120	-340 ± 210	1.6

macroscopic size, such as in Fig. 3. The first contribution coming from peened 5 μm-thick layer does not provide any significant numerical effect if recalculated to the substrate thickness of ~3 mm and therefore can be simply omitted. The second contribution from peening of the coating material is bulk and remains significant. The final recalculation to the conditions imitating real parameters of the coatings where residual stress profile was measured is shown in Fig. 10. Considering finite experimental accuracy the agreement between simulated and experimental data is satisfactory.

The plastic deformation of the particle is generally accepted as a kinetic energy dissipation mechanism. But this generally accounts for a small percentage, approximately 10%, of the overall kinetic energy dissipation. A significant plastic strain gradient is observed in the through thickness of the cladding material and within each particle. The large degree of deformation is closely linked to the non-uniform temperature distribution and thermal softening behaviour introduced through the Johnson–Cook model. The contour maps shown in Fig. 11 show the pronounced plastic strain of the bottom layer with a typical value of 100–200% strain while the top layer shows a much smaller value of 20–50% strain. Such large plastic strains would indicate that significant residual macro-stresses can develop in the cladding/substrate. On the scale of single particle, the core of the particle is much less deformed when compared to the particle's periphery and this can be a source of microstresses. Also apparent and experimentally reported by Assadi [2] is the influence of primary particle morphology on the plastic deformation of subsequent secondary particles. It is apparent that the formation of jets is reliant on the morphology of the underlying substrate as subsequent deposition beyond the first layer sees the particles in the first layer further deform laterally outwards as shown in Fig. 12. This may be linked to cross linking of the particles.

The density measured experimentally on the CS cladding is considerably high, >98%, while average through-thickness density in the simulation is about 80%, as shown in Fig. 13. There might be several reasons for such discrepancy: (i) in the current simulation the deposited particles are sufficiently staggered with no randomisation of the spray and this might provide conditions for predetermined formation of voids, (ii) the density values from simulations were extracted from counting elements in the prescribed boxes (bins) and the procedure of counting is subjected to certain edge effects and box size biasing and this would ultimately influence the absolute values and (iii) the limited number of elements within the model gives rise to inhomogeneous packing upon impact. This can be seen from the fact that the starting element arrangement is regular cubic lattice while at the conclusion of the simulation the model has a glass-like lattice arrangement of particles. Although the limited number of elements does not quite allow for definite conclusion, the four oscillations (isolated maxima in density profile) might suggest that it is due to four distinct deposited layers that produce this variation in density. In reality greater density is achieved through variations in particle size, variable incidence angles, randomised particle arrangements and greater variations in space and time between each particle's deposition. While the authors have noted the lower densities in the simulations, the stresses formed are influenced to a greater extent by the incident particle velocity and the flow stress in the material as opposed to densities and our simulation results reflect this.

9. Discussion

The current simulations shed new light on the micro-mechanical aspects of particle deposition by CS: interaction of an individual particle with the substrate, interaction of multiple particles and the role of temperature-dependent deformation on adhesion of particles. The morphology of CS particles is unequivocally affected by the morphology of the underlying layers, with greater flattening of the primary impacted layers and greater elongation of the secondary particles. Kang et al. [38] outlined the interfacial bonding and microstructural inhomogeneity that arises due to the large temperature and strain gradients. They outlined three phases of the CS process which have been observed within out model: (i) initial primary particle deposition with adiabatic shear instabilities forming in the jetting region with subsequent plastic deformation upon impact by secondary particles, (ii) adiabatic plastic deformation of secondary particles with larger elongated grains and (iii) isothermal heating of the specimens induced by the successive impact of secondary, tertiary and quaternary particles.

In the single-particle study the current authors confirmed typical particle morphology associated with CS (Fig. 5). A number of authors [2,3,30] have noted the correlation between the morphologies and the rapid temperature rise (adiabatic heating) exhibited by a deforming particle in CS. This instability is associated with a thin interface layer with temperatures approaching or exceeding the melting point of the material. Around the particle's periphery (in the jetting region) the temperature is significantly higher than at the centre of the particle as noted from Figs. 6 and 7. Of note is the fact that temperature reaches a maximum value at approximately 40° position from vertical (point F) as seen in Fig. 14. The Von-Mises stress in this jetting region is significantly less than in the neighbouring areas around the particle's periphery. This observation understates the assumption that the thermal softening reduces the flow stress of the material in the jetting zone and overcomes the strain and
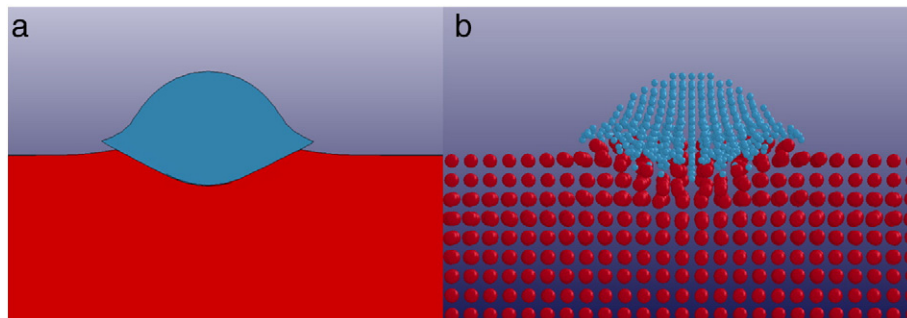
Fig. 5. Single particle shape distortion in the two approaches: (a) the Lagrangian element approach and (b) SPH.
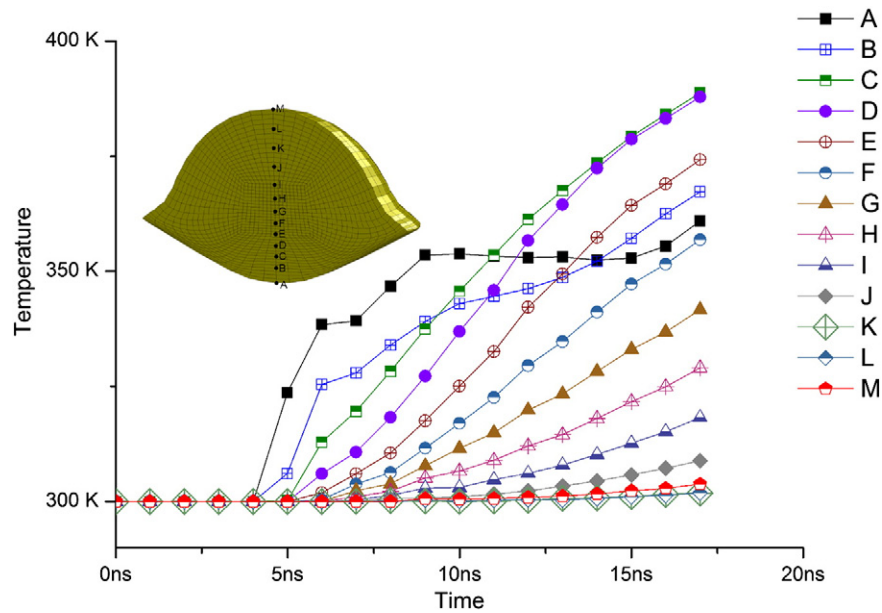
Fig. 6. Thermal history in the through thickness of a single particle obtained with the use of the Lagrangian element approach.

strain-rate hardening. These findings are in line with the findings of other authors [2,3,5,31,33–38].

The main features of multi-particle scenario are similar to a single-particle event. It was observed, that the outer edges of the particles undergo the greatest amount of plastic strain and on the periphery of the particle the deformation is so extreme that jetting of material occurs. Although only four layers of particles were modelled, the multiple particle scenarios establish a distinct difference between the top layer and all others underlying layers in the amount of undergone plastic deformation as shown in Figs. 11 and 12. This clear and apparent result is not surprising, taking into consideration that the particles of the top layer are compacted only by their own kinetic impact while deeper layers are additionally compacted by successive impact of additional particles. However, a through-individual-particle gradient still exists in all particles asserting the hypothesis that even with multiple impacts only surface grains are responsible for particle adhesion. This lends itself to

the study by Kim et al. [40] and Zou et al. [41] who outlined the presence of grain refinement at the periphery of sprayed particles; their study attributed the dynamic recrystallization to the thermal softening of the particle which the current authors believe is a distinct bonding mechanism that can be correlated to the large plastic strains.

The current results further highlight the role of jetting in coating formation. When counted by amount of elements lost in jetting of a single particle experiment vs. overall element losses in full scale multiple-particle experiment then there is a difference and this difference is statistically significant, 7% vs. 3% this is also highlighted in Fig. 12. It appears that the unbounded rapid jetting, observed in the single particle simulation, is demonstratively more suppressed and constrained in the multi particle simulations. It is apparent, that this is due to interaction between neighbouring particles that reduces probability of jetted parts escaping after impact. However the significant inter layer interaction which is seen to influence the radial dispersion of the cold-spray materials may
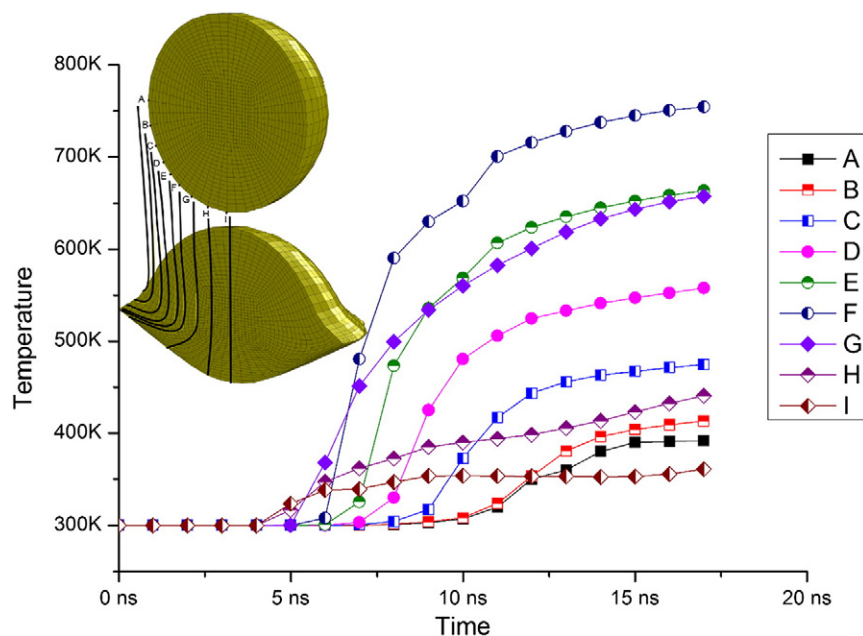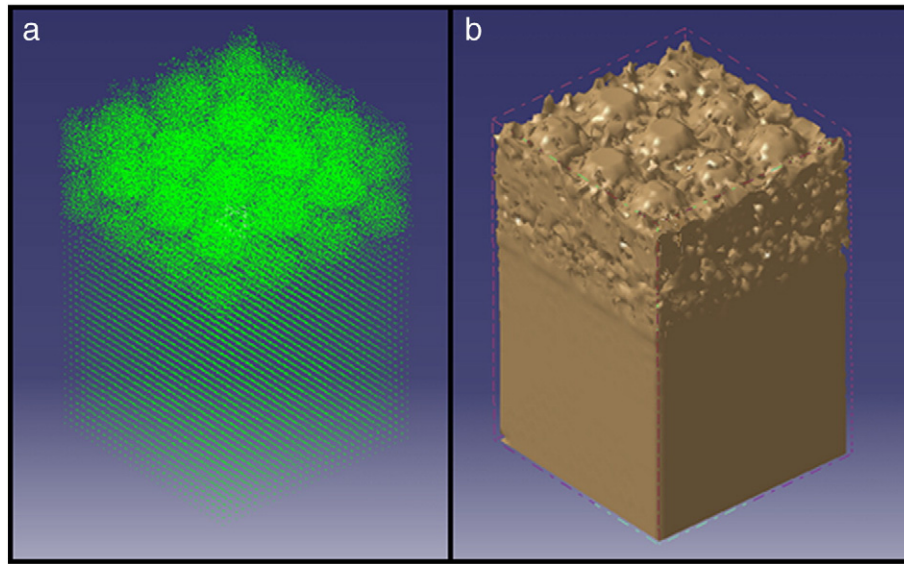

Fig. 7. Thermal history at the periphery of a single particle obtained with the use of the Lagrangian element approach.

Fig. 8. Sample analysed for generation of the through thickness stress profile, visualisation by means of (a) SPH elements and (b) iso-surface.

be the result of the artificially staggered setup and simultaneous impact scenario. In reality particles interact more loosely due to their spatial and time to impact separation. An estimate shows that average distance between particles in the stream is ~50 times larger than the particle size (in the current model the inter-layer distance is ~2 diameter of particle size) which may suggest weak interaction of particle during the real spray process.

Nonetheless jets from neighbouring particles are likely interacting in their semi-molten state; this interaction provides for lateral linkages through metallurgical bonding and mechanical locking upon cooling, or material mixing and diffusion. This can lead to a hypothesis that both the lateral and vertical components of the jetting materials can be partially responsible for the intra and inter layer bonding as jetting materials from neighbouring particles are clearly interacting, thus lending itself to the bonding mechanism of "repeated impacts" [4] whereby the impact of one particle onto another creates more favourable sticking conditions due to increased plastic deformation and further jetting of the CS material.

The authors hypothesise that based on the simulation a likely analogue to the cold sprayed coatings are self-healing metals [32] whereby the liquid metal, with significant alloying elements, becomes an unstable solute. The large stresses may cause cracks that give rise to heterogeneous nucleation. The authors assume that during the impact event stresses can cause small cracks on the surface of both the cold-spray particles and substrate with large free energy surfaces forming at the crack tips. These may span a few atoms in length as noted by Lumley [32], with large dislocation density zones providing a site for heterogeneous nucleation of the alloy's precipitates. The aforementioned cracks may close if enough solute atoms are delivered to these sites; furthermore these may come from neighbouring particles, a process that is analogous to the precipitation forced densification of some sintered materials. This may go some way to explaining the high density of cold-sprayed materials. This hypothesis though requires further analysis and larger models.

Predicted deposition efficiently more than 90%, is seemingly an overestimation in comparison with practical data. There might be several factors influencing this number, such as dispersion of particle velocities, dispersion in the particle impact angle, but probably the most important factor is the oxide layer often found on the surface. While the current constitutive model is used without a damage criterion, it is evident that severe deformations would ultimately lead to the breakdown of the oxide layers exposing internal non-oxidised surfaces that would bolster the bonding mechanism through more efficient liquid metal mixing. As noted earlier the severe deformation is intrinsically linked to the deposition velocity. In the current study only one velocity value was considered as this was used successfully in the physical deposition of the test specimens, but, as noted in other
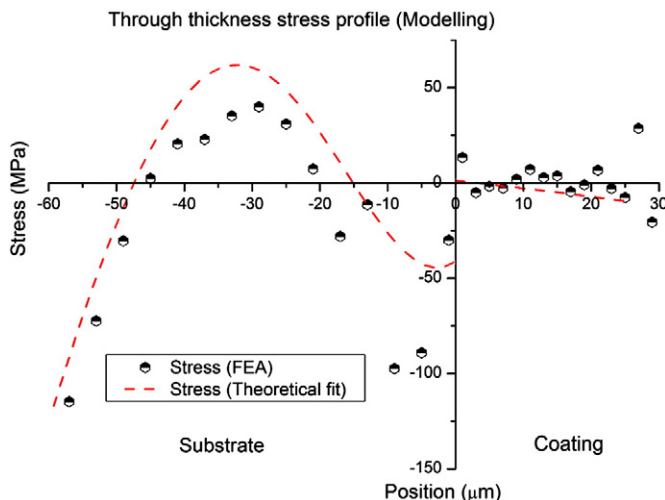
Fig. 9. As-simulated stress profile through 100 μm thick sample.
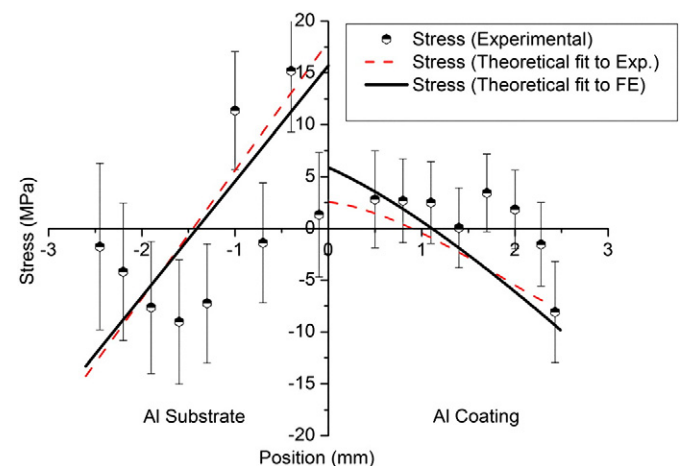
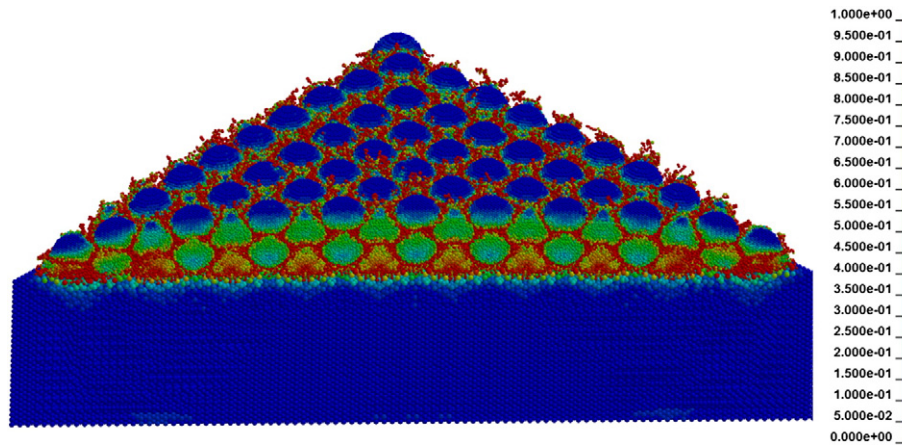**Fig. 10.** Recalculated stress to macroscopically thick, 6 mm, sample.

Fig. 11. Plastic strain contour plot of deposited cold spray particles.

studies [3,5], the successful deposition is reliant on achieving a critical velocity. This warrants further investigation in future studies.

Lastly, the large compressive stress in the substrate at a small distance below the surface is due to the peening effect of the CS particles impacting the substrate surface. At greater depth the stresses become largely tensile in nature owing to the bending being experienced within the substrate to comply with the stress and momentum balance requirements. The compressive residual stress is generally accepted to increase the fatigue life and wear resistance of materials through prevention of stress corrosion cracking. Mahmoudi-Asl [42] demonstrated that moderate compressive stresses (20 MPa) led to a 9% improvement in the fatigue life of cold sprayed magnesium alloys. Conversely, large compressive stresses, approaching yield stresses, can also lead to the coating failures (e.g. through delamination). Analogues to these are seen in shot peening events where increasing the Almen intensity improves the fatigue life of the components up to a critical value; beyond these the materials show a reduction in fatigue life [43]. The question of effective stress control through tuning the spray process parameters and material properties is thus very important. If introduced in desirable quantities, compressive stress generated by CS can be considered as beneficial and hence ensuring a longer component life in corrosion resistance and wear resistance applications.

10. Conclusion

The analysis of the CS particle deposition was successfully carried out using the SPH modelling method demonstrating the particle–particle interaction during deposition and nature of the inter and intra layer adhesion. Overall, the particle deposition mechanism can be characterized as "micro-welding" when each particle is joined to neighbouring ones by a thin band of molten material. Although "microwelding" assumes a thermo-metallurgical mechanism of bonding, the heat source is kinetic in its origin. This view can be corroborated by earlier works on microstructural features of a single particle, experimental studies and via modelling. The large plastic strains are shown to directly correlate with large temperature gradients and these are closely aligned with dynamic recrystallization which is likely occurring at the periphery of all the CS particles.

The Johnson–Cook model along the Mie–Grüneisen EOS, used in the model, were able to account for the adhesive interaction of multiple CS particles, which is absent in many other numerical studies, and allowed the authors to study microscopically thick coating. The adhesion of the CS particles was achieved through the use of the SPH method which
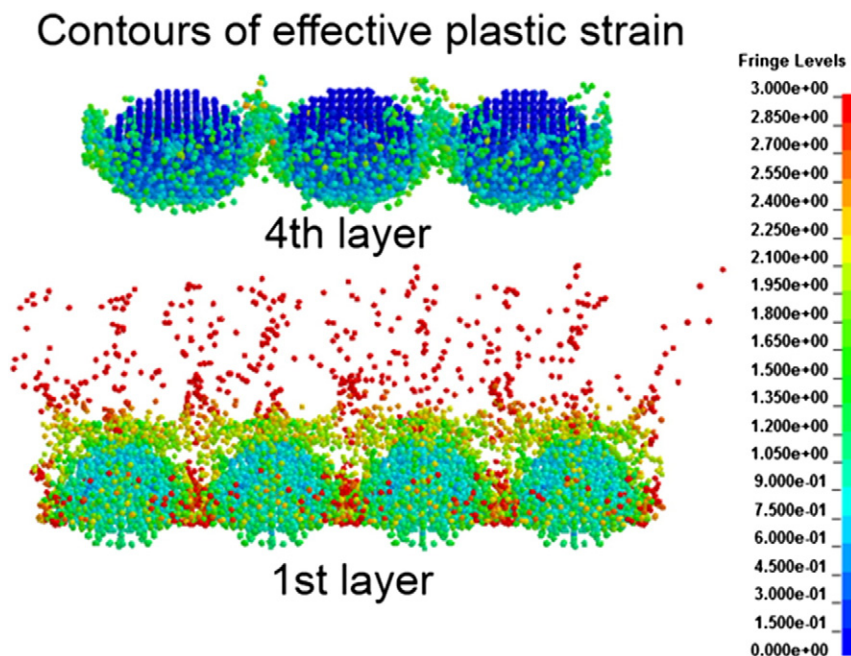

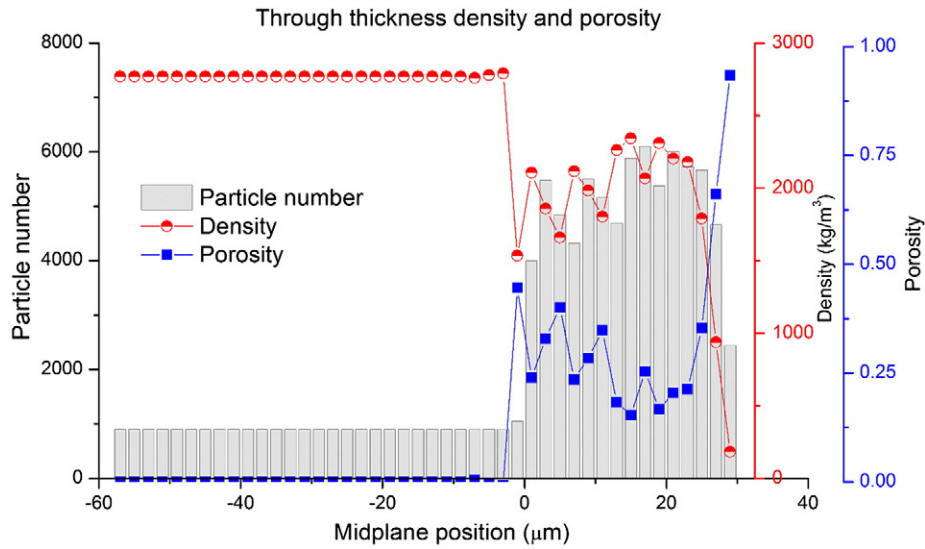**Fig. 12.** Contour maps of plastic strain, side view, in the top and bottom cladding layers.

Fig. 13. Density (porosity) profile through substrate and coating.

would otherwise be problematic to achieve using Lagrangian solid elements.

The major microstructural features, such as particle shape after impact and jetting, were reproduced by the model and contributed to the validation. Along with correct reproducing of the major morphology features, evaluation of the stress state of the materials measured was used for model validation through comparisons with experimental data. The multi-particle deposition scenario allowed for the extraction of experimentally verifiable quantities like residual stress profile. It is apparent that the final stress state is a result of a very fine balance between: (a) dynamic strengthening and the thermal softening of the aluminium alloy and (b) the kinetic impact or shot peening effect upon adhesion of the CS particles. A good agreement between simulated and experimental stress profiles suggests that modelling was able to reproduce main attributes of the CS process. The analysis of the through-thickness stress profiles and the theoretical fit with the Tsui and Clyne empirical model demonstrated the dominance of the kinetic over thermal effects of the deposition process.

One of the major outcomes of the multiple-particle simulation is evaluation of the extent of plastic deformation in CS particles, with a significant difference between the core of an impacted particle and its periphery: with the core exhibiting a lower degree of plastic deformation, while plastic deformation on the periphery of the particle is so severe that local temperature can reach melting point. This localised (adiabatic) heating should be considered pertinent in explaining the adhesion in particular and mechanism of the particle deposition in general.

Acknowledgement

Appendix 1

The SPH method is comprised of two important constituents: (a) kernel approximation of the field functions and (b) the particle approximation. The kernel approximation gives an integral representation of
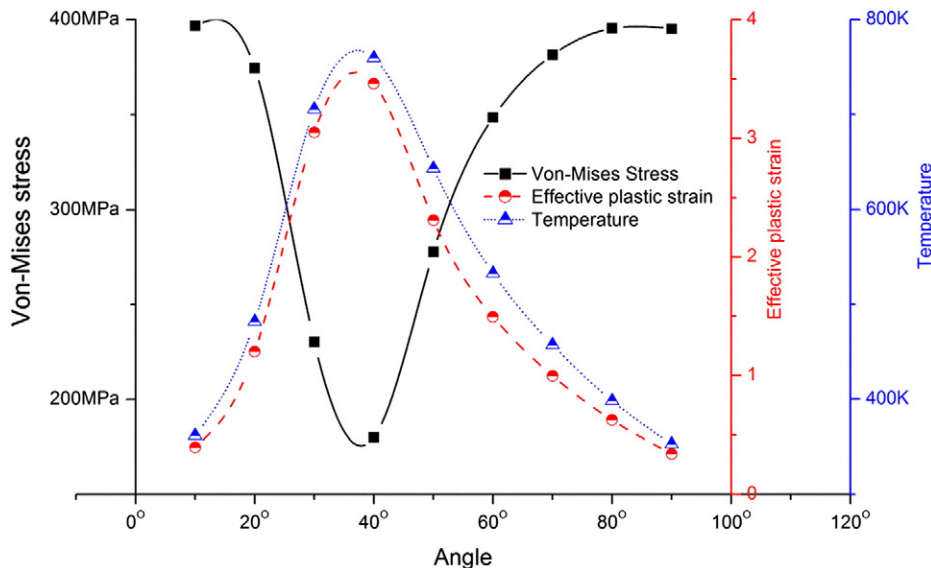

Fig. 14. Temperature, Von-Mises stress and plastic strain around the periphery of the Lagrangian single particle at $t = 17$ ns.
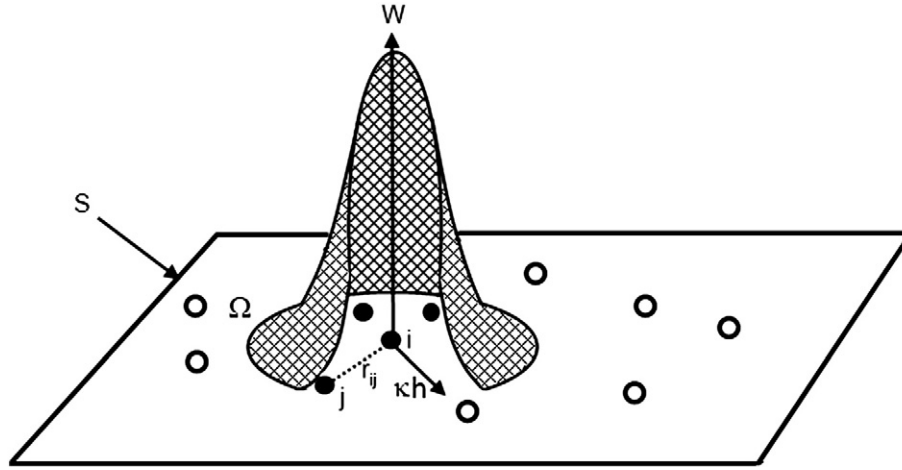
Fig. A1. Kernel approximation and smoothing function.

the field functions, which can be any history variable of interest e.g. pressure, density etc.

The integral representation is given by:

$$f(x) = \int_{\Omega} f(x')\delta(x-x')dx'$$

The function, f, is expressed in terms of the 3D position vector $\mathbf{x}$ and the dirac delta function, $\delta(x - x')$. The function is evaluated over the volume, Ω, of the integral that contains $\mathbf{x}$. The Dirac function can be thought of as a mathematical representation of the instantaneous field variable value if f(x) is defined and continuous in the Ω space.

The Dirac function can be substituted with a smoothing function $W(x - x', h)$. The newly evoked smoothing kernel utilises a smoothing length parameter, h, which dictates the influence area of the smoothing function. Of note is that the approximate relation is second order accurate and is a continuous integral.

The relation thus becomes

$$f(x) = \int f(x')W(x-x',h)dx'.$$

The smoothing function, W, is required to satisfy three conditions (a) the unity condition (b) the compaction condition and (c) the convergence condition which are discussed in detail in [17,18] Many smoothing function are in use in the SPH modelling community but the most common, and often noted, is the cubic or B-spline model used by Monaghan and Lattanzio [19] where:

$$W(x-x',h) = W(R,h) = \alpha_d \times \begin{cases} \frac{2}{3}-R^2+\frac{1}{2}R^3 & 0 \le R<1 \\ \frac{1}{6}(2-R)^3 & 1 \le R<2 \\ 0 & R \ge 2 \end{cases}.$$

The α_d is constant of normalisation and is equal to $5/4h$, $5/\pi h^2$, $105/16\pi h^3$ in the 1-D, 2-D and 3-D space dimensions respectively. The R variable is the relative distance between any two points, $R = \frac{r}{h} = \frac{|x-x'|}{h}$, where r is the distance between two points.

Additional requirements for the smoothing function are

(a) functional symmetry
(b) sufficient smoothness.

The smoothing kernel, as previously mentioned, is continuous but can be approximated using a discrete particle approach using a particle summation over a small volume dx'.

$$f(x) = \int_{\Omega} f(x')W(x-x',h)dx' \approx \sum_{j=1}^{N} f\left(x_j\right)W\left(x-x_j,h\right)V_j$$

where, $V_j = \frac{m_j}{\rho_j}$ is the finite volume and is expressed in terms of the mass of particle j, m_j, and the particle density, ρ_j. The approximate function for particle i can thus be written as:

$$f(x_i) = \sum_{j=1}^{N} \frac{m_j}{\rho_j} f\left(x_j\right)W\left(x_i-x_j,h\right) = \sum_{j=1}^{N} \frac{m_j}{\rho_j} f\left(x_j\right)W_{ij}$$
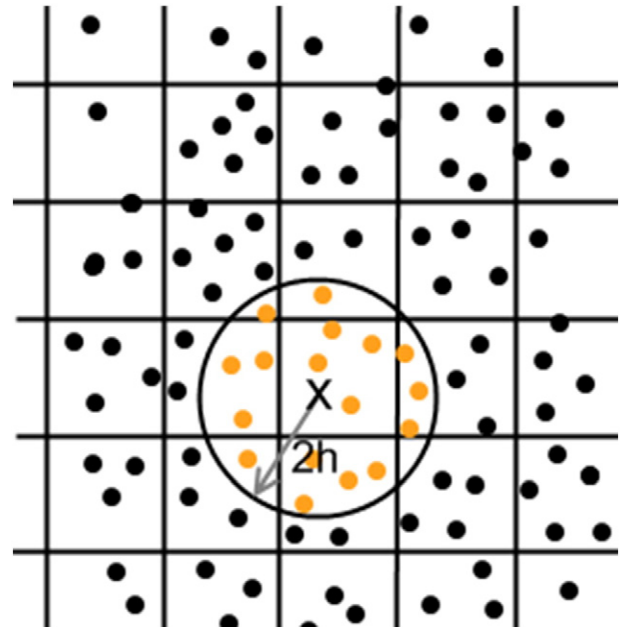

Fig. A2. SPH neighbouring particle search algorithm in LS-DYNA.

where N is the number of particles, W_{ij} is the smoothing function of particle i evaluated at particle j and is expressed in terms of the relative distance R_{ij} and

$$W_{ij} = W\left(x_i - x_j, h\right) = W\left(\left|x_i - x_j\right|, h\right) = W\left(R_{ij}, h\right).$$
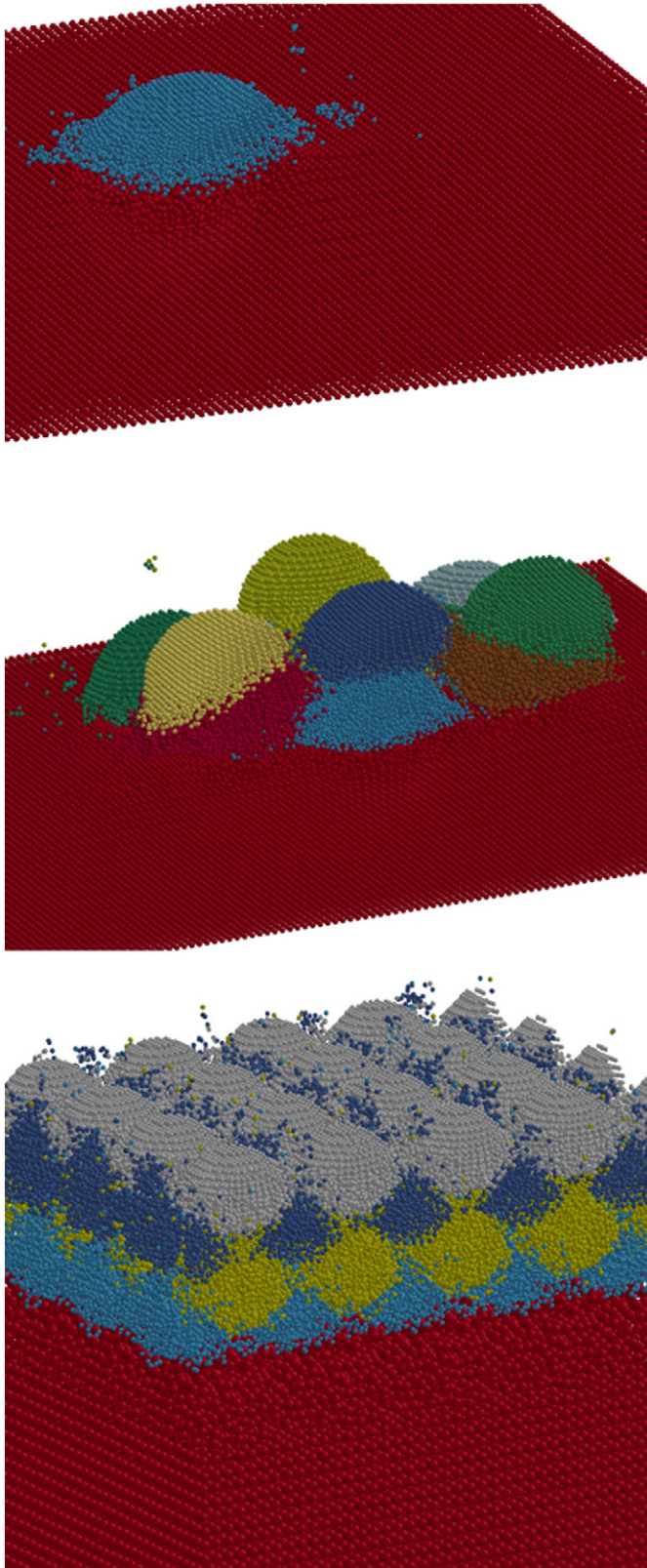

Fig. A3. Development of multi-particle SPH model.

Fig. A1 shows a pictorial representation of the aforementioned smoothing and kernel functions.

Appendix 2

The sphere of influence around each particle is defined by a radius equal to 2 h, where h is the smoothing length. The purpose of the search is to compute the interaction between each particle at each time step. The search for neighbouring particles for a random set of M particles would result in M(M − 1) neighbour searches. This is often a limiting factor to consider when meshing as a large numbers of elements as it would quickly overwhelm the numerical computation.

The SPH search algorithm within LS-DYNA uses a system analogous to that of the bucket sort algorithms used in the contact card within LS-DYNA, Fig. A2. The analysis domain is discretised into boxes each containing a number of SPH elements. The boxes are smaller than the sphere of influence hence the neighbour search only looks for neighbouring particles within the immediate box and then within neighbouring boxes which fall within the 2 h radius limit. This method helps alleviate the problems associated with unbounded searches with the number of distance computation reducing from M(M − 1) to approximately M(logM).

The use of a constant smoothing length has been noted to be problematic for both large compressive and tensile forces. In the first instance the large number of particles within the 2 h influence spheres would effectively make any large simulations ineffective as the number of neighbouring particles, and consequently the number of neighbour searches increases rapidly. In the second instance with large tensile stresses the distance becomes too large, reducing the number of neighbouring particles and making the simulation more prone to instabilities and inaccuracies. It's thus advantageous to maintain a relatively consistent number of neighbouring particles by using variable smoothing length. The variable smoothing length is evaluated by using the following relation:

$$\frac{dh}{dt} = \frac{1}{3} \cdot h \cdot div(v)$$

where $div(v)$ is the divergence of the flow speed. To function correctly the user is required to enter an upper (h_{max}) and lower (h_{min}) scaling factors. The LS-DYNA default values are 0.2 and 2.0 respectively. $h_{min} \times h_0 < h < h_{max} \times h_0$, where h_0 is the initial smoothing length.

With respect the SPH simulations a number of models were run with increasing number of particles and elements as shown in Fig. A3. The model's stability and run times were recorded with varying kernel approximations and smoothing functions. The resultant model is based on the capacity of an 8-cpu Linux cluster running version 971 R5.0 of LS-DYNA. The resultant run time was 163 h, to ensure minimal fluctuations in the stresses to mimic a spring back type simulation.

References

[1] W.Y. Li, C. Zhang, C.L. Li, H. Liao, J. Therm. Spray Tech. 18 (5–6) (2009) 921–933.
[2] H. Assadi, F. Gartner, T. Stoltenhoff, H. Kreye, Acta Mater. 51 (2003) 4379–4394.
[3] G. Bae, Y. Xiong, S. Kumar, K. Kang, C. Lee, Acta Mater. 56 (2008) 4858–4868.
[4] S.G. Klinkov, V.F. Kosarev, M. Rein, Aerosp. Sci. Technol. 9 (2005) 582–591.
[5] M. Grujicic, J.R. Saylor, D.E. Beasley, W.S. Derosset, D. Helfritch, Appl. Surf. Sci. 219 (2003) 21–227.
[6] K. Spencer, V. Luzin, M. Zhang, Mater. Sci. Forum 654–656 (2010) 1880–1883.
[7] Y.C. Tsui, T.W. Clyne, Thin Solid Films 306 (1997) 23–33.
[8] W.Y. Li, H.L. Liao, C.J. Li, G. Li, C. Coddet, X.F. Wang, Appl. Surf. Sci. 253 (2006) 2852–2862.
[9] S. Sampath, X.Y. Jiang, J. Matejicek, L. Prchlik, A. Kulkarni, A. Vaidya, Mater. Sci. Eng. A 364 (2004) 216–231.
[10] S.J. Howard, Y.C. Tsui, T.W. Clyne, Pro. of the 7th National Thermal Spray Conf. Boston. USA, 1994.
[11] D.J. Greving, J.R. Shadley, E.F. Rybicki, J. Therm. Spray Tech. 3 (1994) 371.
[12] R.T.R. McGrann, D.J. Greving, et al., J. Therm. Spray Tech. 7 (4) (1998) 546–552.
[13] V. Luzin, K. Spencer, N. Matthews, J. Davis, M. Saleh, THERMEC Conf. Proc, Quebec city, Canada, 2011.

[14] M. Vesenjal, Z. Ren, J. Serb. Soc. Comp. Mech. 1 (2007) 74–86.
[15] L.D. Cloutman, Report No. UCRL-ID-105520. LLNL, 1991.
[16] C. Espinosa, J.L. Lacome, J. Limido, M. Salaun, C. Mabru, R. Chiergatti, 10th Int. LS-DYNA Users Conf. Michigan, USA, 2008.
[17] R.A. Gingold, J.J. Monaghan, Mon. Not. R. Astron. Soc. 181 (1977) 375–389.
[18] L.B. Lucy, Astron. J. 82 (1977) 1013–1024.
[19] J.J. Monaghan, J.C. Lattanzio, Astron. Astrophys. 149 (1985) 135–143.
[20] J. Hallquist, Livermore Software Technology Corporation, Livermore, CA, 2011.
[21] E.A. Flores-Johnson, M. Saleh, L. Edwards, Int. J. Impact Eng. 38 (12) (2011) 1022–1032.
[22] M.B. Liu, G.R. Liu, Arch. Comput. Meth. Eng. 17 (2010) 25–76.
[23] G.R. Johnson, W.H. Cook, Proc. 7th Int. Symp. On Ballistics, The Netherlands, 1983, pp. 541–547.
[24] G.H. Majzoobi, R. Azizi, A. Alavi Nia, J. Mater. Process. Technol. 164–165 (2005) 1226–1234.
[25] Y. Hu, C. Gong, Z. Yao, J. Hu, Surf. Coat. Technol. 203 (23) (2009) 3503–33508.
[26] D.R. Lesuer, G.J. Kay, M.M. LeBlanc, Report. UCRL-JC-134118, LLNL, 2001.
[27] D. Steinberg, Report. UCRL-MA-106439 LLNL, 1996.
[28] The MathWorks Inc, Massachusetts, 2011.
[29] S. Diehl, Rockefeller, C.L. Fryer, Report. LA-UR-08-5763. LANL, 2008.
[30] Papyrin, A (Ed), Elsevier Publishing. (2007).
[31] W.Y. Li, S. Yin, X.F. Wang, Appl. Surf. Sci. 256 (2010) 3725–3734.
[32] R.N. Lumley, Mater. Forum 31 (2007).
[33] Shuo Yin, Xiao-fang Wang, Wen-ya Li, Bao-peng Xu, J. Therm. Spray Tech. 18 (4) (2009) 686–693.
[34] S. Gu, S. Kamnis, Metall. Mater. Trans. A 40A (2009) 2664–2674.
[35] T. Hussain, D.G. McCartney, P.H. Shipway, D. Zhang, J. Therm. Spray Tech. 18 (3) (2009) 364–379.
[36] T. Schmidt, H. Assadi, F. Gartner, H. Richter, T. Stoltenhoff, H. Kreye, Thomas Klassen, J. Therm. Spray Tech. 18 (5–6) (2009) 794–808.
[37] R.C. Dykhuizen, M.F. Smith, D.L. Gilmore, R.A. Neiser, X. Jiang, S. Sampath, J. Therm. Spray Tech. 8 (4) (1999) 559–564.
[38] K. Kang, J. Won, G. Bae, S. Ha, C. Lee, J. Mater. Sci 47 (2012) 4649–4659.
[39] T.S. Duffy, T.J. Ahrens, J. Geophys. Res. 97 (1992) 4503–4520.
[40] K. Kim, M. Watanabe, J. Kawakita, S. Kuroda, Scr. Mater. 59 (2008) 768–771.
[41] Y. Zou, W. Qin, E. Irissou, J.G. Legoux, S. Yue, J. Szpunar, Scr. Mater. 61 (2009) 899–902.
[42] Mahmoudi-Asl, H M.A. Thesis, U of Waterloo, Canada, 2011.
[43] M. Hilpert, L. Wagner, in: K.U. Kainer (Ed.), WILEY-VCH, 2000, pp. 463–468.
[44] K. Heritage, C. Frisby, A. Wolfenden, Rev. Sci. Instrum. 59 (6) (1988) 973–974.
[45] K. Spencer, V. Luzin, N. Matthews, M. Zhang, Surf. Coat. Technol. 206 (2012) 4249–4255.
[46] V. Luzin, K. Spencer, M.X. Zhang, Acta Mater. 59 (3) (2011) 1259–1270.
[47] E. Kröner, Z. Phys. A Hadrons Nucl. 151 (1958) 504–518.
[48] W.B. Choi, L. Li, V. Luzin, R. Neiser, T. Gnäupel-Herold, H.J. Prask, S. Sampath, A. Gouldstone, Acta Mater. 55 (3) (February 2007) 857–866.